aerospace

MDPI

Article

Reduced-Order Model for Performance Simulation and Conceptual Design of Rocket-Type Pulse Detonation Engines

Luis Sanchez de Leon [1], Francisco Sastre [1], Elena Martin [2] and Angel Velazquez [1,*]

[1] Fluid Mechanics and Aerospace Propulsion Department, Universidad Politécnica de Madrid, 28040 Madrid, Spain; luis.sanchezdeleon@upm.es (L.S.d.L.); francisco.sastre@upm.es (F.S.)
[2] Institute of Physics and Aerospace Sciences IFCAE, School of Aeronautics and Space Engineering, Universidad de Vigo, Campus Ourense, 36004 Ourense, Spain; emortega@uvigo.es
* Correspondence: angel.velazquez@upm.es

Abstract: A model-based method has been developed for the performance simulation and conceptual design of rocket-type pulse detonation engines (PDEs). A reduced-order model (ROM) has been generated based on the high order singular value decomposition of a data tensor obtained from CFD computations. This ROM could be used to solve the direct (performance) and inverse (design) problems in the context of the early phases of pulse detonation engine design. Output performance parameters are predicted from prescribed input operation/geometry parameters in the direct problem, and vice versa in the inverse problem. The focus of this method is industrial application in situations where large parametric searches are to be performed with a reasonable level of fidelity at a low computational cost. It was found that the performance and conceptual design tool thus developed provides results that deviate, on average, by less than 10% from the CFD results. Regarding practical implementation, the method allows for shifting the heavier computational load off-line. In this way, when working on-line, the user can obtain results in less than a second for every single case. The main contribution of this study is showing that a model-based approach that combines CFD and tensor decomposition has the potential to extract a maximum of information from a given computational effort. This characteristic makes the method of interest for early design phases in the aerospace industry.

Keywords: pulse detonation engine; conceptual design; performance

Academic Editors: Yunfeng Liu and Zhiwu Wang

Received: 30 December 2024
Revised: 29 January 2025
Accepted: 6 February 2025
Published: 10 February 2025

Citation: Sanchez de Leon, L.; Sastre, F.; Martin, E.; Velazquez, A. Reduced-Order Model for Performance Simulation and Conceptual Design of Rocket-Type Pulse Detonation Engines. *Aerospace* **2025**, *12*, 132. https://doi.org/10.3390/aerospace12020132

1. Introduction

Nowadays, the interest in pulse detonation engines (PDEs) is growing. The reasons for this could be their high propulsive performance, relatively low engineering complexity, and flexibility in addressing a wide variety of requirements. The fields of application of PDEs include aeronautics, space propulsion, and energy generation. The main characteristic of the PDE (also referred to as pulse detonation thruster, PDT) thermodynamic cycle is that the combustion front is supersonic (detonation wave). In this way, a constant-volume addition of heat that yields highest thermodynamics cycle efficiency is approached. The level of technical maturity in the field could be ascertained from the recent ground firing tests reported by Buyakofu et al. [1], and the subsequent flight testing of a PDE performed by the same team, Buyakofu et al. [2]. Also, it is relevant to mention the recent experimental work reported by Bogoi et al. [3], Cojocea et al. [4], and Oh et al. [5].

Conceptual design and performance methods are needed for propulsion plants that have reached a certain level of development. The reason for this is the need to explore large

multi-dimensional spaces that take operating parameters into account with reasonable fidelity at an affordable computational cost. Typically, the performance study of a propulsion plant may involve the computation of hundreds, even thousands, of cases. This wealth of information may provide guidelines for detailed experimental testing and/or high-fidelity numerical studies. Also, it can assist in the process of making decisions regarding system engineering aspects.

A starting point for the review of conceptual design and performance studies of PDEs could be chapter 5.12 of the book by Mattingly [6]. In this reference, an idealized description of the PDE thermodynamic cycle is presented and discussed in a comprehensive way. Regarding models with a higher level of complexity, Ma et al. [7] combined analytical and numerical analyses to address the propulsive performance of an airbreathing PDE. Their chemical kinetics model was based on a one-step reaction with a single process variable. Wintenberger and Shepherd [8] developed a simplified flow-path analysis of an airbreathing PDE. The authors presented an analytical method to predict engine performance. It was based on an open-system control volume analysis. Endo and Fujiwara [9] presented a PDE model structured into three modules: combustion, exhaust, and filling. The combustion and exhaust modules were analyzed with a simplified model based on: (a) the Hugoniot relation for the Chapman–Jouguet detonation wave and (b) a self-similar approach for the rarefaction waves. Mitrofanov and Zhdan [10] published a study in which they analyzed the thrust performance of an idealized PDE. They considered that air and combustion products behave as ideal gases with a constant ratio of specific heats, and that an instantaneous heat release simulates the detonation wave phenomenon. Under these assumptions, they found a superior thrust performance of the PDE as compared with the scramjet and one-spool turbojet concepts.

Allgood et al. [11] systematically varied the length-to-diameter ratio of a PDE in their experiments. They found that the thrust performance depends strongly on the operating fill fraction and proposed a new dimensionless parameter in their analysis, incorporating said fill fraction. Li et al. [12] studied a formulation based on a constant-volume cycle model combined with a chemical equilibrium model. Paxon [13] presented an idealized model for detonation-based constant-volume combustors. The author combined simple algebraic chemical kinetics modelling with a quasi-1D Euler solver and concluded that the results were not very far off from those obtained with higher-fidelity flow solvers. Paxon and Kaeming [14] concentrated on the influence of unsteadiness. Chen et al. [15] carried out an idealized thermodynamic analysis to assess the potential gain of using pulse detonation combustion in the bypass duct of a turbofan.

Recently, Peace and Lu [16] developed a quasi-1D model, based on the method of characteristics, to evaluate the flow field and the propulsive performance of a PDE. The authors explicitly expressed their aim of developing a computationally inexpensive model. To this aim, they considered simplifications that were specific to isentropic flow fields. For example, they assumed that entropy changes occurred at discontinuities only. The obtained results were compared with a variety of numerical and experimental studies (see figures 12–19 of their article). The authors found that their quasi-1D method was accurate enough to be used with confidence in performance studies. Qiu et al. [17] also used a 1D model to analyze the performance of an air-breathing PDE under a large variety of operating conditions. Their model was based on an ideal thermal cycle in which the ideal pressure ratio was obtained theoretically. In this case, spatial discretization was achieved via the advection upstream splitting method, and temporal discretization was achieved via a third-order Runge–Kutta approach. The chemical source term was formulated by using the Strang-splitting method. Asli et al. [18] developed a 1D method for the performance evaluation of turbines driven by pulse detonation combustion. Their method involved the use of Euler equations with

blade source terms, while the turbine model was addressed by implementing a steady-state mean-line analysis. The authors recognized that their assumption of a 1D approach to modelling a 3D problem implies a strong idealization. Interestingly, they found that nearly half of the unsteadiness (irrespective of its actual fluctuation) was damped throughout the first blade row. Tan et al. [19] considered a zero-dimensional model to study the transient operating characteristics of a pulse detonation turbine engine (PDTE). One of the main assumptions that the authors made about their model was a superposition of quasi-steady and dynamics modes of behavior. It is interesting that, in spite of their model being zero-dimensional, they reported that their method, which needs to be solved iteratively in time via two loops, deviates by less than 10% from experimental results obtained in a prototype PDTE. Xiao et al. [20] performed a theoretical energy and exergy analysis of a pulse detonation combustor in the context of analyzing a pulse detonation turbine engine cycle. They considered the use of iso-octane (C_8H_{16}) as fuel within a simplified exergy flow model that was compared to the case of an isobaric combustion chamber. Even though they used an idealized model that was compared to another simplified model, they provide useful insights regarding the functional dependencies of the thermodynamics cycle.

The present manuscript describes a method that could be used for conceptual design and performance studies of a rocket-type PDE. The method might be used both in its direct and inverse approaches. In the direct approach, prescribed geometry and operating input parameters allow for the computation of output performance parameters (i.e., the "performance" problem). In the inverse problem, prescribed output performance parameters allow for the computation of input geometry and operating parameters that are consistent with said performance (i.e., the "design" problem). The novelty of this development is that it increases the model fidelity (1D CFD including detailed 10-species chemical kinetics plus a simulation of the blowdown phase) while retaining the very fast response time (less than a one tenth of a second) of a typical algebraic zero-dimensional method. This is achieved by solving the conceptual design and/or performance problem not on the PDE model itself, but on a reduced-order model of the database that represents the PDE. This reduced-order model (ROM) is based on the high order singular value decomposition (HOSVD) technique. In this way, the computational load of database generation and mode/pattern recognition via HOSVD is shifted off-line. Then, conceptual design and/or performance maps of the system can be generated in a matter of minutes. In rocket-type PDEs, the nozzle is a critical component. However, since this study is of a methodological nature, it has been decided to keep the exposition of the methodology as simple as possible. As a result, the presence of a nozzle has not been considered.

Regarding manuscript organization, the problem is described in Section 2; a global overview and a detailed description of the methodology are presented in Sections 3 and 4, respectively; the results are presented and discussed in Section 5; and, finally, conclusions are given in Section 6.

2. Problem Description

The idealized PDE could be considered as a cylinder of constant diameter. Fresh propellants are injected at one end. The other end remains open to produce thrust. The thermodynamic cycle of the PDE can be summarized in four distinct phases.

Filling: Fresh propellants with a prescribed mixture ratio are injected into the tube, which is filled with an inert gas, from the closed end. In the ideal case, propellants are perfectly mixed.

Ignition: Supersonic detonation starts at the closed end and travels along the cylinder. This phase ends when the detonation wave reaches the open end, and hot compressed gases start to exit to the surrounding ambient environment.

Exhaust: Behind the detonation wave, combustion products, at a very high pressure and temperature, are ejected from the cylinder, generating thrust.

Purging: Below a certain pressure threshold, injection re-opens, and an inert gas is used to purge the cylinder of combustion products from the previous detonation.

In the present study, a PDE model was generated that could be visualized as two sets of input and output parameters. Inputs, P1–P6 are related to the geometry, configuration, and operation of the PDE:

- P1: initial gas temperature inside the PDE, T_0 [K];
- P2: equivalence ratio, ϕ;
- P3: initial flow pressure inside the PDE, P_0 [bar];
- P4: PDE length, L [m];
- P5: PDE diameter, D [m];
- P6: relaxation time between detonations, t_{off} [s], which includes both purging and re-filling.

Outputs, Q1 to Q7, were PDE performance parameters:

- Q1: initial gas temperature inside the PDE, T_0 [K];
- Q2: total impulse per cycle, I_T [Ns];
- Q3: specific impulse, I_{sp} [m/s];
- Q4: detonation working frequency, $Freq.$ [Hz];
- Q5: peak thrust, E_{max} [N];
- Q6: peak pressure, P_{max} [bar];
- Q7: total ejected mass per cycle, M_T [kg].

The objective was the development of a method that could solve the PDE direct problem (prescribed input parameters leading to the computation of output parameters: "performance") and the inverse problem (prescribed output parameters leading to the computation of input parameters: "design"). For practical reasons, the initial temperature, T_0, was considered as an input for the direct problem, and as an output for the inverse problem.

The development was undertaken in the context of the method's application to the preliminary design phases of PDEs. In these early phases, the conceptual design and performance need to be addressed by means of exploring large multi-dimensional spaces that incorporate design, operating, and performance parameters. Therefore, the method needs to be robust, reasonably accurate, and inexpensive in terms of the required computational load. In the remainder of the manuscript, this is called the DPA (design and performance algorithm).

In this study, the PDE was expected to be designed and operated within certain ranges of the input parameters, P1–P6. Their actual ranges are shown in Table 1.

Table 1. Ranges of the input parameters.

Parameter	Range
T_0 [K]	250–350
P_0 [bar]	0.5–10
ϕ	0.5–1.05
L [m]	0.4–1.5
D [m]	0.01–0.25
t_{off} [s]	0–0.1

3. Global Overview of the Methodology

The methodology was developed along two lines: (1) the PDE model (organized into two steps: numerical simulation and data reduction), and (2) the DPA (organized into three steps: database generation, database decomposition, and inverse problem solution). Line 1 is specific to the actual system being studied (the PDE). Line 2 is generic and could

be applied to any other system provided that a suitable direct problem model is available for said system.

3.1. PDE Model

The PDE model was organized into two steps (steps 1 and 2 of the workflow).

- Step (1) Numerical simulation: The flow solver had a 1D formulation, in line with previous developments, such as those by Peace and Lu [16], Hua et al. [17], and Asli et al. [18]. However, its level of fidelity was increased by means of implementing: (a) a 10-species and 25-reactions chemical kinetics model, and (b) a discharge to a low ambient pressure. A total number of 480 simulations were run;
- Step (2) Data reduction: The results of the 480 simulations were generalized as closed-form dimensionless analytical relations. The dimensionless parameters that made up these relations were selected by means of dimensional analysis. In a general case, these relations may not be available; in this situation, Step 2 is skipped and the workflow proceeds to Step 3.

3.2. DPA Algorithm

The DPA algorithm was organized into three steps (steps 3, 4, and 5 of the workflow).

- Step (3) Database generation: The closed-form data reduction relations were used to generate the PDE database (if these were not available, simulation results from Step 1 would be used instead, albeit at the cost of a much less populated database). The database form was that of seven 6D tensors. The dimensions of each tensor corresponded to the six input parameters P1–P6. Each tensor contained, stored as data, one of the seven output parameters Q1–Q7;
- Step (4) Database decomposition. The HOSVD technique was used to decompose the aforementioned tensors, with the objective being to identify the eigenmodes (patterns) that retain most of the information contained in the database.
- Step (5) Inverse problem solution. The formulation of the solution had the global character of an optimization approach. It was based on closed-form analytical expressions of the densified eigenmodes.

To facilitate the use of the methodology by industrial and/or institutional users, the DPA was translated into an app. It has a visual interface and can be used both for direct (performance) and inverse (design) problems. Steps 1–4 were performed off-line since these needed to be executed only once. The app deals with Step 5 alone, which is the one that works on-line. For this purpose, the app pre-loads the results generated off-line from Step 4. The app's response time for a single calculation (either for the direct or for the inverse problem) is of the order of hundredths of a second. This allows the user to generate performance and/or design maps within minutes. The methodology thus developed is generic and could be applied to cases with a larger number of parameters, or with simulations with a higher level of fidelity.

3.3. Workflow

A visual impression of the workflow described in Sections 3.1 and 3.2 is presented in Figure 1.

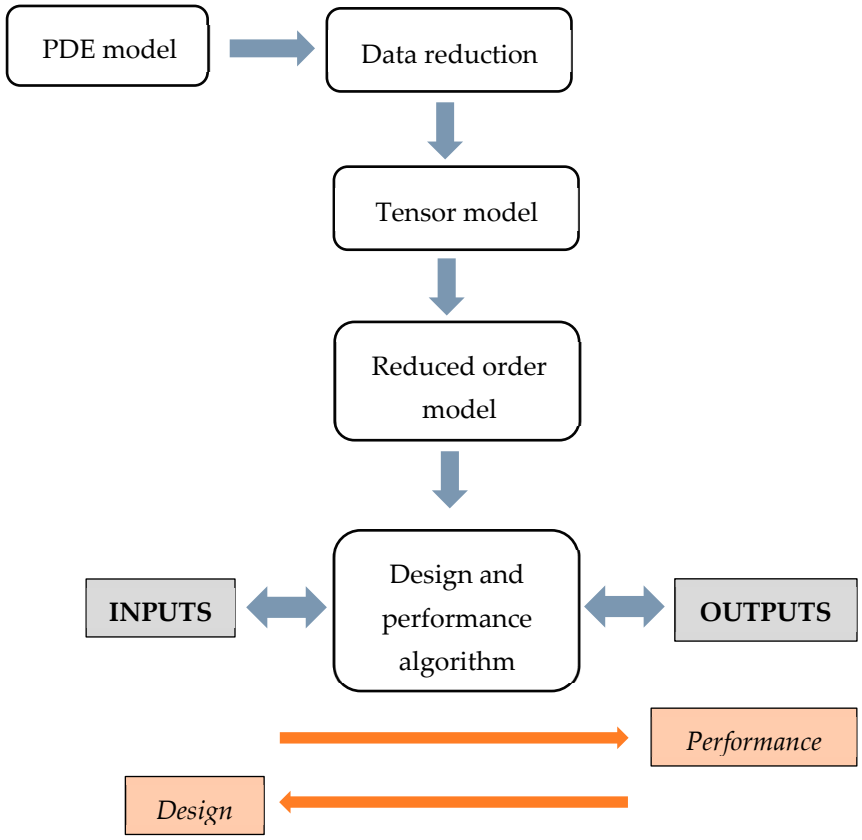

Figure 1. Methodology workflow.

4. Detailed Description of the Methodology

4.1. Step 1: PDE Model, Numerical Simulation

The problem under consideration was 1D. The results obtained, valid for a 1 m^2 cross-section, were scaled to the actual cylindrical cross-section area of the PDE. The working fluids were H_2 and air. The phases simulated using CFD were: (a) ignition (detonation wave propagation inside the tube) and (b) exhaust (blowdown of burned gases to the ambient environment). Figure 2 shows a sketch of the computational domain. A closed end is present at $x = 0$, and an open end is present at $x = L$. The shaded area of length 0.2% L represents the initial ignition region.

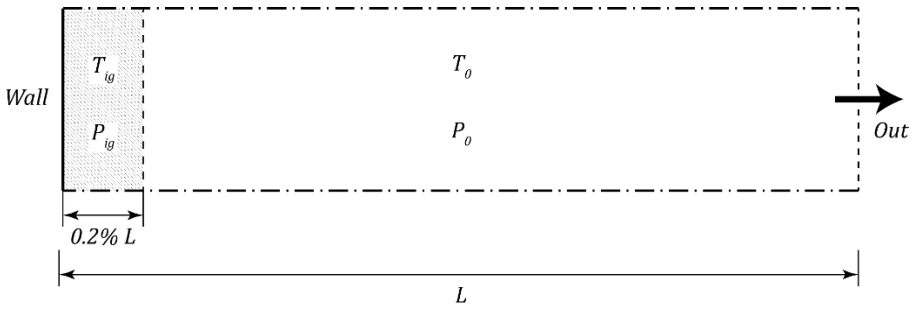

Figure 2. Sketch of the 1D computational domain. The shaded region whose length is 0.2% L indicates the initial ignition region.

The flow was described by compressible reactive Euler equations. The conservative variables were the density of the gas mixture, ρ, the linear momentum, ρu, the total energy, ρE, and the species densities, ρY_k (Y_k represents the mass fraction of each species k in the mixture). The specific total energy E is defined as $E = h_s - p/\rho + u^2/2$, where the sensible enthalpy, h_s, is related to the temperature, T, as follows:

$$h_s = \int_{T_0}^{T} \sum_{k=1}^{N} c_{p_k}^{o} \frac{Y_k}{W_k} \, dT \tag{1}$$

W_k is the molecular weight of each k species, and $c_{p_k}^{0}$ the species' molar constant pressure heat capacities obtained from JANAF polynomials ($a_{j,k}$ coefficients).

$$c_{p_k}^{o} = R_u \sum_{j=1}^{5} a_{j,k} T^{j-1} \tag{2}$$

The relation between the pressure and density in the mixture of N ideal gases was modelled by the state equation as follows:

$$p = \sum_{k=1}^{N} p_k = T \rho R_u \sum_{k=1}^{N} \frac{Y_k}{W_k} \tag{3}$$

where R_u is the universal gas constant. The source term, $\dot{\omega}_T$, in the energy equation is given by $\dot{\omega}_T = \sum_{k=1}^{N} \dot{\omega}_k \, \Delta h_{f_k}^{o}$, where $\dot{\omega}_k$ and $\Delta h_{f_k}^{o}$ are, respectively, the production/consumption rates of each species and, for each species, the formation enthalpy obtained from the JANAF polynomials. The H_2-air chemical kinetics mechanism used was the one proposed by Marinov et al. [21]. This model has been used by other researchers in detonation problems, i.e., Gutiérrez Marcantoni et al. [22]. The mechanism involves $N = 10$ species and $M = 25$ elementary reactions. The reactions used and their respective (forward) Arrhenius coefficients are listed in Table 2. They can be divided into four categories: (a) chain reactions, (b) H_2/O_2 dissociation/recombination reactions, (c) the formation and consumption of HO_2, and (d) the formation and consumption of H_2O_2.

Table 2. Arrhenius coefficients for the Marinov et al. [21] H_2-air chemical kinetics model. Third body efficiencies for reactions 17 and 18 are given at the bottom. Units are in s, mol, cm^3, cal, and K, respectively.

	Reaction		A	b	E_a
1	$OH + H_2 \rightleftarrows H + H_2O$		$2.14 \cdot 10^8$	1.52	3449.0
2	$O + OH \rightleftarrows O_2 + H$		$2.02 \cdot 10^{14}$	−0.4	0.0
3	$O + H_2 \rightleftarrows OH + H$		$5.06 \cdot 10^4$	2.67	6290.0
4	$H + O_2(+M) \rightleftarrows HO_2(+M)$		$4.52 \cdot 10^{13}$	0.0	0.0
		Low:	$1.05 \cdot 10^{19}$	−1.257	0.0
5	$H + O_2(+N_2) \rightleftarrows HO_2(+N_2)$		$4.52 \cdot 10^{13}$	0.0	0.0
		Low:	$2.03 \cdot 10^{20}$	−1.59	0.0
6	$H + O_2(+H_2) \rightleftarrows HO_2(+H_2)$		$4.52 \cdot 10^{13}$	0.0	0.0
		Low:	$1.52 \cdot 10^{19}$	−1.133	0.0
7	$H + O_2(+H_2O) \rightleftarrows HO_2(+H_2O)$		$4.52 \cdot 10^{13}$	0.0	0.0
		Low:	$2.10 \cdot 10^{23}$	−2.437	0.0
8	$OH + HO_2 \rightleftarrows H_2O + O_2$		$2.13 \cdot 10^{28}$	−4.827	3500.0
8b	$OH + HO_2 \rightleftarrows H_2O + O_2$		$9.10 \cdot 10^{14}$	0.0	10,964.0
9	$H + HO_2 \rightleftarrows OH + OH$		$1.50 \cdot 10^{14}$	0.0	1000.0
10	$H + HO_2 \rightleftarrows H_2 + O_2$		$8.45 \cdot 10^{11}$	0.65	1241.0
11	$H + HO_2 \rightleftarrows O + H_2O$		$3.01 \cdot 10^{13}$	0.0	1721.0
12	$O + HO_2 \rightleftarrows O_2 + OH$		$3.25 \cdot 10^{13}$	0.0	0.0
13	$OH + OH \rightleftarrows O + H_2O$		$3.57 \cdot 10^4$	2.4	−2112.0
14	$H + H + M \rightleftarrows H_2 + M$		$1.00 \cdot 10^{18}$	−1.0	0.0
15	$H + H + H_2 \rightleftarrows H_2 + H_2$		$9.20 \cdot 10^{16}$	−0.6	0.0

Table 2. *Cont.*

	Reaction	A	b	E_a
16	$H + H + H_2O \rightleftarrows H_2 + H_2O$	$6.00 \cdot 10^{19}$	-1.25	0.0
17 *	$H + OH + M \rightleftarrows H_2 + M$	$2.21 \cdot 10^{22}$	-1.25	0.0
18 *	$H + O + M \rightleftarrows OH + M$	$4.71 \cdot 10^{18}$	-1.0	0.0
19	$O + O + M \rightleftarrows O_2 + M$	$1.89 \cdot 10^{13}$	0.0	-1788.0
20	$HO_2 + HO_2 \rightleftarrows H_2O_2 + O_2$	$4.20 \cdot 10^{14}$	0.0	11,982.0
20a	$HO_2 + HO_2 \rightleftarrows H_2O_2 + O_2$	$1.30 \cdot 10^{11}$	0.0	-1629.0
21	$OH + OH(+M) \rightleftarrows H_2O_2(+M)$	$1.24 \cdot 10^{14}$	-0.37	0.0
	Low:	$3.04 \cdot 10^{30}$	-4.63	2049.0
	Troe : 0.470 ; 100.0 ; 2000.0 ; 10^{15}			
22	$H_2O_2 + H \rightleftarrows HO_2 + H_2$	$1.98 \cdot 10^{6}$	2.0	2435.0
23	$H_2O_2 + H \rightleftarrows OH + H_2O$	$3.07 \cdot 10^{13}$	0.0	4217.0
24	$H_2O_2 + O \rightleftarrows OH + HO_2$	$9.55 \cdot 10^{6}$	2.0	3970.0
25	$H_2O_2 + OH \rightleftarrows H_2O + HO_2$	$2.40 \cdot 10^{0}$	4.042	-2162.0

* $\{R_{17}, R_{18}\} = \{H_2O = 6.4\}$.

Regarding the initial conditions, the cylinder was filled with a fresh H_2-air mixture with a constant equivalence ratio, ϕ; static pressure, P_0; and static temperature, T_0. The detonations were numerically triggered by setting a small initial ignition region at a high ignition temperature, $T_{ig} = 2000\ K$, and high ignition pressure, $p_{ig} = \alpha\ P_0$. The selection of the ignition pressure p_{ig}, defined by parameter α, was critical in obtaining sustained detonations. α was selected as follows:

$$\alpha(\phi, p_0) = n_1 \left[1 + \left(\frac{\phi_1 - \phi}{\phi_2 - \phi_1} \right) \left[\frac{e^{-P_0/p_{ref}} - e^{-p_1/p_{ref}}}{e^{-p_2/p_{ref}} - e^{-p_1/p_{ref}}} \right] \right] \tag{4}$$

with $n_1 = 56$, $\phi_1 = 0.5$, $\phi_2 = 1.05$, $p_{ref} = 1$ bar, $p_1 = 0.5$ bar, and $p_2 = 10$ bar.

This relation (4) has not been tested for other mixtures. It is valid for H_2-air only, and only within the parametric range of this study. Regarding the boundary conditions, zero velocity was prescribed, and the gradient was set to zero for the other variables (p, T, and mass fractions) at $x = 0$. Two different conditions were prescribed at $x = L$ depending on the flow stage: a) during the propagation of the detonation wave, zero gradient was imposed at the outlet for all variables, and b) once the detonation wave reached the tube outlet, a discharge of the gases (blowdown) to the ambient pressure was considered. The idealized "1D nozzle" throat was choked since the pressure inside the tube was very high when compared with the ambient pressure. Then, the velocity at the outlet section was adjusted to match the sound velocity at all times. The blowdown regime was computed until the static pressure of the flow at the closed end of the cylinder reached the initial pressure p_0, and the chemical model was deactivated during this blowdown phase, to speed up the simulation.

The set of flow equations and the chemical kinetics model, together with the prescribed initial and boundary conditions, were solved via a finite volume method in the open-source CFD software OpenFOAM® using the density-based solver rhoCentralRfFoam, as per Gutiérrez Marcantoni et al. [22]. A second-order central-upwind scheme was selected for the discretization of the convective terms because of its smaller numerical dissipation. As the chemical reaction source terms lead to a stiff system of equations, a time splitting method, which alternates between solving the homogeneous conservation laws without source terms (i.e., the fluid flow) and solving the conservation laws without convection (i.e., the chemistry), was used. The selected algorithm was the semi-implicit Bader and Deuflhard [23] version of the SIBS algorithm.

The following global variables were obtained from the computations: thrust, $F_x(t)\ \left[\mathrm{N/m^2}\right]$; mass flow at the open end of the PDE, $\dot{m}(t)\ \left[\mathrm{kg/(sm^2)}\right]$; mass inside the

PDE, $M(t)$ $[\mathrm{kg/m^2}]$; average flame velocity, $\overline{FV}$ $[\mathrm{m/s}]$; total impulse, $I_t = [\mathrm{kg(m/s)/m^2}]$; and specific impulse, I_{sp} $[s]$.

The maximum Courant number for all simulated cases was 0.15. A sensitivity analysis was performed, shown in Table 3, to select both the cell size and temporal discretization scheme. Five different mesh sizes, 0.125 mm, 0.167 mm, 0.250 mm, 0.333 mm, and 0.500 mm, and three numerical schemes, the Euler implicit (EI), backward second-order (B), and Crank Nicolson (CN) schemes, were considered. The final selection, based on a compromise between stability, computational time, and accuracy, was a cell size of 0.250 mm and the Euler implicit scheme.

Table 3. Sensitivity of results with regard to mesh size and temporal discretization scheme ($\boldsymbol{\phi = 1, L = 0.4}$ m, $\boldsymbol{P_0 = 1}$ bar, $\boldsymbol{T_0 = 300}$ K). Temporal discretization schemes (TDSs): Euler implicit (EI), backward second-order (B), Crank Nicolson (CN). Cases $\boldsymbol{\Delta x = 0.125}$ mm (EI) and $\boldsymbol{\Delta x = 0.250}$ mm (CN) are taken as references for comparison with other cases.

Δx[mm]	TDS	$\overline{FV}$[m/s]	Deviation	I_{sp}[s]	Deviation
0.500	EI	1996	0.5%	153	0
0.333	EI	1982	0.2%	152	0.6%
0.250	EI	1983	0.2%	153	0
0.167	EI	1984	0.1%	153	0
0.125	EI	1986	*Reference*	153	*Reference*
0.250	EI	1983	0.2%	153	0.6%
0.250	B	1988	0.1%	154	0
0.250	CN	1986	*Reference*	154	*Reference*

Concerning solver validation, five cases were computed and compared with the experimental and analytical results of Shauer et al. [24] and Wintenberger et al. [25]. The variable used for comparison was the specific fuel-based impulse. It was computed as a function of the equivalent ratio, ϕ, for the following prescribed parameters: $P_0 = 1$ bar, $T_0 = 300$ K, $L = 0.7$ m. The actual comparison is presented in Figure 3. The numerical results of the present model correlate well with the experimental data of Schauer et al. [24] for equivalence ratios larger than 0.6. For the stoichiometric mixture, $\phi = 1$, the results differ by less than 2%. The qualitative trend of the numerical results agrees well, also, with the analytical results of Wintenberger et al. [25]. Concerning the flame velocity, Schauer et al. [24] reported 1959 m/s for ϕ = 1, while Soloukhin [26] reported 1968 m/s. The present simulation yields 1991 m/s, which is within a band of 2% around the results of references [24,26].

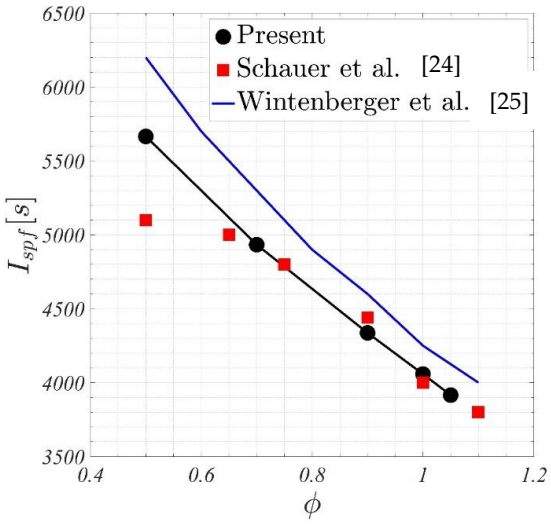

Figure 3. Black dots: present results. Red squares: Schauer et al. [24], experimental. Blue line: Wintenberger et al. [25], analytical. $\boldsymbol{I_{spf}}$ is the fuel-based specific impulse.

4.2. Step 2: Data Reduction

Since the CFD simulations were 1D (extensive variables were calculated per unit area) and only the detonation and blowdown phases were modelled, only four parameters (P1–P4) needed to be discretized (treatment of cylinder diameter and cycle time is addressed in Section 4.3). The discretization of the input variables for the CFD simulations is shown in Table 4, amounting to a total of 480 cases.

Table 4. CFD input parameters.

Parameter	Discretization	Number of Values
T_0 [K]	250, 300, 350	3
P_0 [bar]	0.5, 0.75, 1, 2, 4, 6, 8, 10	8
ϕ	0.5, 0.7, 0.9, 1, 1.05	5
L [m]	0.4, 0.7, 1.0, 1.5	4

A process of data reduction was carried out to generalize the results obtained in these 480 simulation cases. A dimensional analysis was performed first. Then, a trial-and-error procedure was used to seek the functional relations of the dimensionless variables that collapse the data in the most compact form. New dimensionless independent variables, dependent variables, and global parameters were defined following relations (5), (6), (7a), and (7b) as follows:

$$\widetilde{x} = \frac{x}{L},\ \widetilde{t} = \frac{t}{\phi^{\frac{-3}{8}} L/\sqrt{q}} \tag{5}$$

$$\widetilde{\rho} = \frac{\rho}{\phi^{-1} M_f/L},\ \widetilde{u} = \frac{u}{\phi^{\frac{3}{8}}\sqrt{q}},\ \widetilde{p} = \frac{p}{\phi^{\frac{-1}{4}} M_f\, q/L},\ \widetilde{T} = \frac{T}{\phi^{\frac{3}{4}}\, q/R_{g,0}} \tag{6}$$

$$\widetilde{F}_x = \frac{F_x}{\phi^{\frac{-1}{4}} M_f\, q/L},\ \widetilde{\dot{m}} = \frac{\dot{m}}{\phi^{\frac{-5}{8}} M_f\, \sqrt{q}/L},\ \widetilde{M} = \frac{M}{\phi^{-1} M_f} \tag{7a}$$

$$\widetilde{I} = \frac{I_t}{\phi^{\frac{-5}{8}} M_f \sqrt{q}},\ \widetilde{t}_{wave} = \frac{t_{wave}}{\phi^{\frac{-3}{8}} L/\sqrt{q}},\ \widetilde{t}_{end} = \frac{t_{end}}{\phi^{\frac{-3}{8}} L/\sqrt{q}},\ \widetilde{FV} = \frac{\overline{FV}}{\phi^{\frac{3}{8}}\sqrt{q}} \tag{7b}$$

M_f is the initial mass of fuel (per square meter) inside the cylinder, and q is the total heat released during detonation (calculated by means of the JANAF coefficients, depending on the initial mixture inside the cylinder, and assuming complete combustion of the reactants) divided by the initial mass of fuel inside the cylinder. t_{wave} is the time needed by the detonation wave to reach the end section of the PDE ($x = L$). t_{end} is the total time of the simulation, accounting for the propagation of the detonation wave plus the blowdown phase, as described above.

The scaling parameters, L, q, $R_{g,0}$, M_f, and ϕ, in relations (5), (6), (7a), and (7b) were selected to make the dimensionless variables as independent as possible of the initial conditions P_0 and T_0. In this respect, the following aspects should be highlighted:

- Parameters q and $R_{g,0}$ depend only on the equivalence ratio (ϕ) of the initial mixture;
- The selected reference velocity $\phi^{\frac{3}{8}}\sqrt{q}$ depends only on ϕ. If the Chapman–Jouguet velocity, V_{CJ}, is chosen as the reference velocity instead of $\phi^{\frac{3}{8}}\sqrt{q}$, an unwelcome dependency on the initial mixture temperature would appear;
- The scaling temperature depends only on the equivalence ratio ϕ;
- M_f, which depends on the equivalence ratio and on the PDE length, is the only parameter that depends on the initial mixture conditions via the ratio P_0/T_0.

Figures 4–6 show $\widetilde{I}$ versus $\widetilde{P}_0$, $\widetilde{t}_{end}$ versus $\widetilde{P}_0$ (non-dimensional initial pressure in the cylinder), and $\widetilde{FV}$ versus ϕ, respectively. The actual plots of the 480 results (solid dots) suggest that simple analytical relations (dashed black lines) could be fitted to them. In

particular, $\widetilde{I}$ and $\widetilde{FV}$ happen to be constant, while $\widetilde{t}_{end}$ correlates linearly with $\widetilde{P}_0$. The analytical expressions for the fitting curves are:

$$\widetilde{I} = \varphi_1 = 4.9 \tag{8}$$

$$\widetilde{t}_{end} = \varphi_2\left(\widetilde{P}_0\right) = -353.8\,\widetilde{P}_0 + 46.3 \tag{9}$$

$$\widetilde{FV} = \varphi_3 = 0.19 \tag{10}$$

where φ_1, φ_2, and φ_3 denote functional relations.

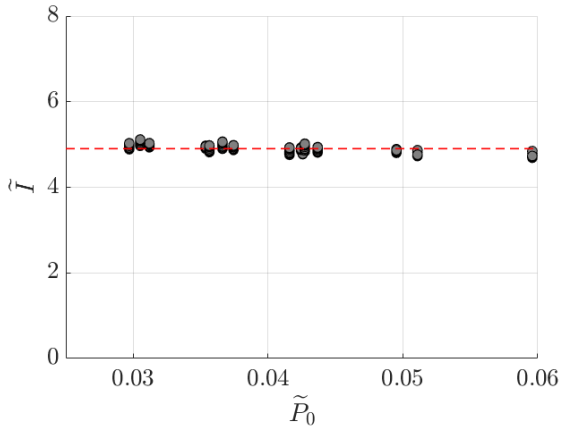

Figure 4. $\widetilde{I}$ versus $\widetilde{P}_0$. Solid dots: 480 dimensionless CFD results. Dashed red line: fitting relation (8).

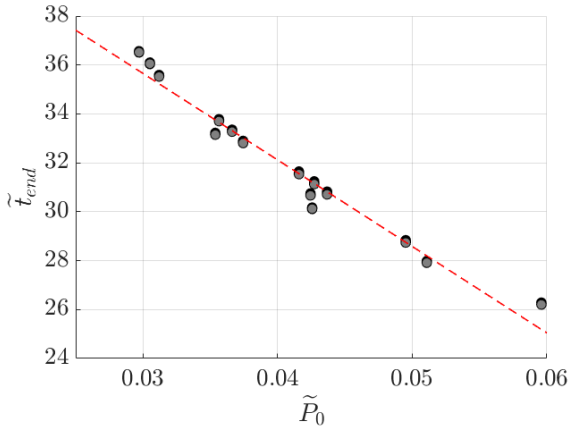

Figure 5. $\widetilde{t}_{end}$ versus $\widetilde{P}_0$. Solid dots: 480 dimensionless CFD results. Dashed red line: fitting relation (9).

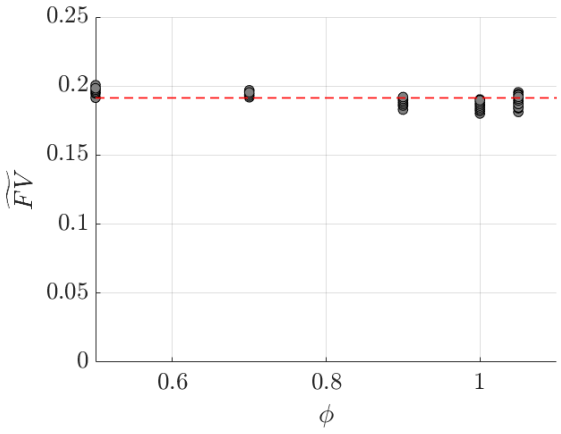

Figure 6. $\widetilde{FV}$ versus ϕ. Solid dots: 480 dimensionless CFD results. Dashed red line: fitting relation (10).

The evolution of the dimensionless thrust, $\widetilde{F}_x$, versus the dimensionless time, $\widetilde{t}$, is shown in Figure 7. It could be observed that the 480 numerical profiles collapse into a single curve.

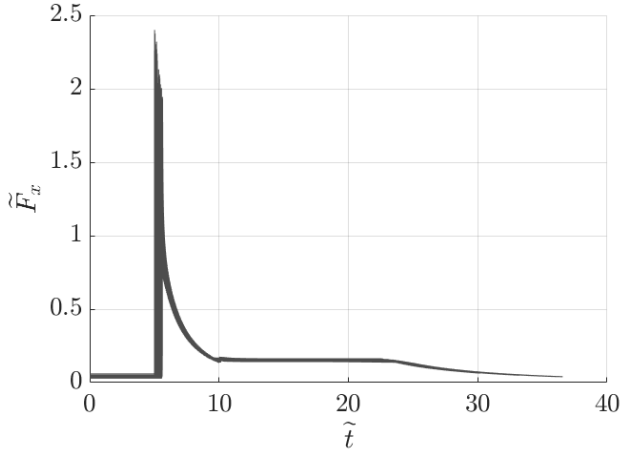

Figure 7. $\widetilde{F}_x$ vs. $\widetilde{t}$ for all 480 computed cases.

Then, the evolution of the thrust and, similarly, of any other time-dependent dimensionless variable could be described using the dimensionless relation:

$$\widetilde{F}_x = \varphi_4\left(\widetilde{t}\right) \tag{11}$$

where φ_4 denotes a functional relation. The appropriate dimensionless temporal evolution function, e.g., $\varphi_4\left(\widetilde{t}\right)$ for the thrust performance, is obtained by rendering dimensionless the numerical results generated for just one CFD case. The same process can be applied to obtain the dimensionless fields $\widetilde{p}\left(\widetilde{x}, \widetilde{t}\right)$, $\widetilde{T}\left(\widetilde{x}, \widetilde{t}\right)$, $\widetilde{u}\left(\widetilde{x}, \widetilde{t}\right)$, and $Y_k\left(\widetilde{x}, \widetilde{t}\right)$.

4.3. Step 3: Database Generation

Data reduction relations (8), (9), (10), and (11) were used to densify the databases of performance variables. A relaxation time, t_{off} (input parameter P6), was defined to account for the purging and refilling phases of the PDE cycle (not considered in the CFD simulations) plus any downtime in which the user might deliberately choose not to operate the PDE. Hence, the complete cycle time, t_{cycle}, was $t_{cycle} = t_{end} + t_{off}$.

This cycle time was used to approximate the working frequency of the PDE when it was operated continuously. Additionally, the cylinder diameter, D (input parameter P5), was defined at this point to convert the CFD results per unit area (thrust in N/m^2, mass in kg/m^2, etc.) back to their usual dimensional form (thrust in N, mass in kg, etc.) by means of characterizing the actual PDE cross-sectional area $(\pi/4)D^2$. With these adjustments, a new function based on the data-reduction relations, f_{DR}, to compute the Q1–Q7 outputs of the PDE model from the P1–P6 inputs, could be defined in the general form:

$$\left(T_0, I_T, I_{sp}, Freq, E_{max}, P_{max}, M_T\right) = f_{DR}\left(T_0, P_0, \phi, L, D, t_{off}\right) \tag{12}$$

The set of databases of densified input parameters, shown in Table 5, was created using the data reduction laws. Each of them contained 11 × 11 × 12 × 12 × 9 × 11 = 1,724,976 data. Since seven output parameters, Q1–Q7, were considered, the total number of data in the databases was 1,724,976 × 7 = 12,074,832. The computational time for the 480 CFD cases was 14 days. Generation of the densified databases required 10 h.

Table 5. Values of the densified input parameters.

Parameter	Discretization	Number of Values
T_0 [K]	250:10:350	11
P_0 [bar]	0.5:0.95:10	11
ϕ	0.5:0.05:1.05	12
L [m]	0.4:0.1:1.5	12
D [m]	0.01:0.03:0.25	9
t_{off} [s]	0:0.01:0.1	11

4.4. Step 4: Reduced-Order Model and Direct Problem

The data contained in the densified databases were rescaled as follows:

$$\hat{Y} = \frac{Y - Y_{min}}{Y_{max} - Y_{min}} \tag{13}$$

where Y_{max} and Y_{min} were the tensor maximum and minimum values, respectively. The rationale for relation (13) was to work with values of variables ranging from 0 to 1. The 6D tensors were aggregated into a single 7D tensor that was decomposed via HOSVD. Details about this decomposition can be found in Tucker [27] and De Lathauwer et al. [28]. The form of the decomposition is given in relation (14).

$$T_{i_1 i_2 \ldots i_N} = \sum_{i'_1=1}^{I_1} \sum_{i'_2=1}^{I_2} \cdots \sum_{i'_N=1}^{I_N} S_{i'_1 i'_2 \ldots i'_N} U^1_{i_1 i'_1} U^2_{i_2 i'_2} \ldots U^N_{i_N i'_N} \tag{14}$$

S is the core tensor that contains the eigenvalues of the decomposition. The U^i values are the matrices that contain the eigenmodes. Each U^i matrix corresponds to one input parameter. Cubic splines were fitted to each one of the eigenmodes and stored along with the core tensor, S. For the spline fitting, the input parameters were normalized as in relation (13); namely:

$$\hat{X} = \frac{X - X_{min}}{X_{max} - X_{min}} \tag{15}$$

where X_{max} and X_{min} were the maximum and minimum values of each input parameter. At this point, all required information was stored in the core tensor and in the splines. This, together with the tensor product (14), allowed for any combination of inputs to deliver the corresponding set of outputs. Any single case of the HOSVD-based reduced-order model represented by relation (16) took 0.04 s to compute in a ASUS Dual GeForce RTX 4070 OC Edition 12GB, Taipei, Taiwan.

$$\left(T_0, I_T, I_{sp}, Freq, E_{max}, P_{max}, M_T\right) = f_{HOSVD}\left(T_0, P_0, \phi, L, D, t_{off}\right) \tag{16}$$

4.5. Step 5: Inverse Problem

The inverse problem involved the determination of the set of input (operation and geometry) parameters that yielded a prescribed set of output (performance) parameters. That is, the inverse problem is the design problem. To address this, a gradient-based optimization method was selected. The associated workflow required the iterative solution of the direct problem, which was obtained using the ROM.

The finding of the solution of the inverse problem started with the prescription of a set of output parameters, referred to as the "query". The objective was to identify the input parameters that aligned with this query, based on the ROM. The optimization method applied in this study used an interior-point algorithm for constrained minimization. It was implemented within Matlab's 'fmincon' suite. Constraints were imposed at the ROM's boundaries, with a tolerance of ±5%. The objective function minimized the Euclidean distance between the ROM-computed outputs and the query.

To ensure an effective starting point for the optimization process, a pre-generated list of 500 sample points was stored alongside the ROM. These sample points, generated using the Latin hypercube sampling technique, were distributed evenly across the six-dimensional parameter space. Each sample point included a set of input values and their corresponding output values. The optimal starting point was identified as the input set that produced the output closest to the query, as determined by the Euclidean distance.

Once the initial point was established, the iterative optimization process was started, according to the methods proposed by Byrd et al. [29,30] and Waltz et al. [31]. Each iteration step required the computation of the Jacobian and Hessian matrices to obtain the Lagrangian matrix, making extensive use of the ROM. On average, the ROM was executed 300 times per single inverse problem. The computational time, using parallel computing, was 0.4 seconds per case.

5. Results

To test the methodology, both for the direct and inverse problems, 50 CFD test cases were chosen at random within the parametric range defined in Table 4. None of these test cases coincided with any of the 480 CFD simulations used for the development of the ROM.

5.1. Direct Problem

The ROM was used to compute the direct problem using the test cases. The performance variables obtained with the ROM were compared with the CFD results. To this end, the error was defined as follows:

$$Y_{err} = \left|\hat{Y}_{CFD} - \hat{Y}_{ROM}\right| \tag{17}$$

where the subscripts "CFD" and "ROM" refer to numerical simulation and reduced-order model results, respectively. Because of the selected normalization, shown in relation (13), the error defined in (17) had the character of a relative error.

$$Y_{err} = \left|\hat{Y}_{CFD} - \hat{Y}_{ROM}\right| = \left|\frac{Y_{CFD} - Y_{min}}{Y_{max} - Y_{min}} - \frac{Y_{ROM} - Y_{min}}{Y_{max} - Y_{min}}\right| = \left|\frac{Y_{CFD} - Y_{ROM}}{Y_{max} - Y_{min}}\right| \tag{18}$$

An error vector of seven components was obtained for each test case, corresponding to the seven output parameters. The mean error per variable is shown in Figure 8. For all performance parameters, the mean error was less than 10%. The maximum mean errors (between 5% and 10%) occurred for the specific impulse and peak cycle pressure. The mean errors for the other parameters were less than 2%. In current industrial practice, these errors are acceptable for performance studies in conceptual design phases.

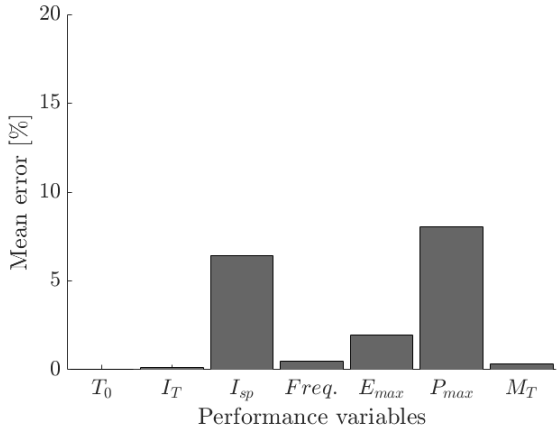

Figure 8. Mean error per variable of the direct problem.

The distribution of the mean error per test case was computed and the results are represented as a histogram in Figure 9. The distribution is centered on an error of 2.5% and the maximum mean error was 6.2%, which, again, is acceptable for industrial applications.

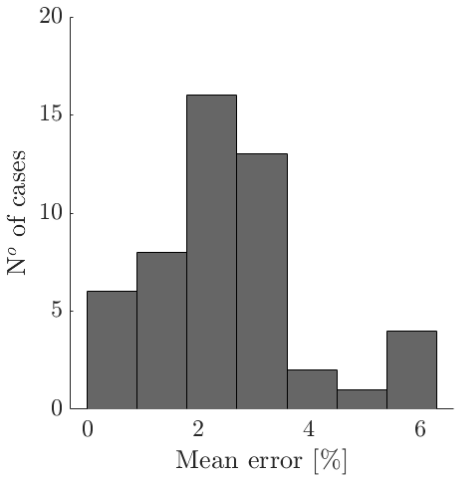

Figure 9. Distribution of the mean error per test case in the direct problem.

5.2. Inverse Problem

The 50 test cases mentioned in the previous section, Section 5.1, were used, also, to compute the inverse problem. The error between the input parameters in the test case and the ROM solution was quantified using an approach similar to the one presented in the previous section, see relations (17) and (19).

$$X_{err} = \left| \hat{X}_{test\_case} - \hat{X}_{ROM} \right| \tag{19}$$

The counterpart of Figure 8, for the reverse problem, is represented in Figure 10. In this case, the parameters that presented the larger errors were the initial pressure, equivalence ratio, and PDE length. In any case, the errors were always smaller than 10%. The counterpart of Figure 9, for the incerse problem, is presented in Figure 11. In this case, the distribution is centered on an error of 3.6% and the maximum mean error was 6.6%. As in the case of the direct problem, these errors are acceptable in the context of pre-design conceptual studies.

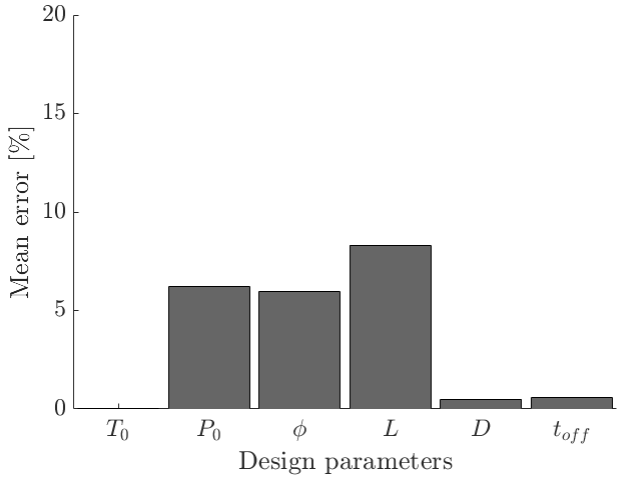

Figure 10. Mean error per variable of the inverse problem.

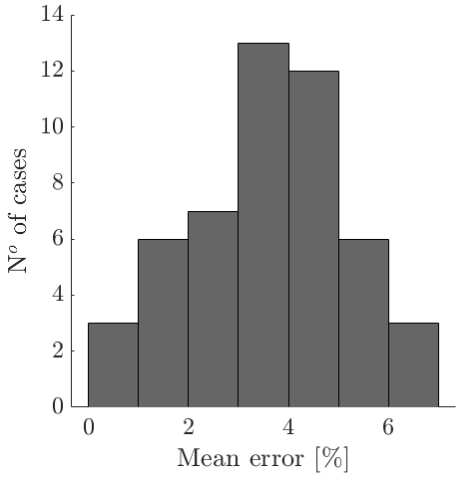

Figure 11. Distribution of the mean error per test case in the inverse problem.

5.3. Application Case: Data Reduction Relations

As a typical case, the following set of input parameters was considered: $\phi = 0.7$, $L = 0.75$ m, $P_0 = 5.5$ bar, $T_0 = 280$ K. These parameters were not included in the matrix of 480 CFD cases, shown in Table 4. The spatial-temporal evolution of the pressure field is presented and compared to the CFD results in Figure 12. It could be observed that the CFD profiles of the space- and time-dependent pressure are very close to those obtained via the data reduction relations. The CFD-computed values of I_t and t_{end} were 5402 Ns/m^2 and 0.00250 s. The results obtained using the data reduction functions were 5374 Ns/m^2 and 0.00251 s. The deviations were 0.5% and 0.4%, respectively.

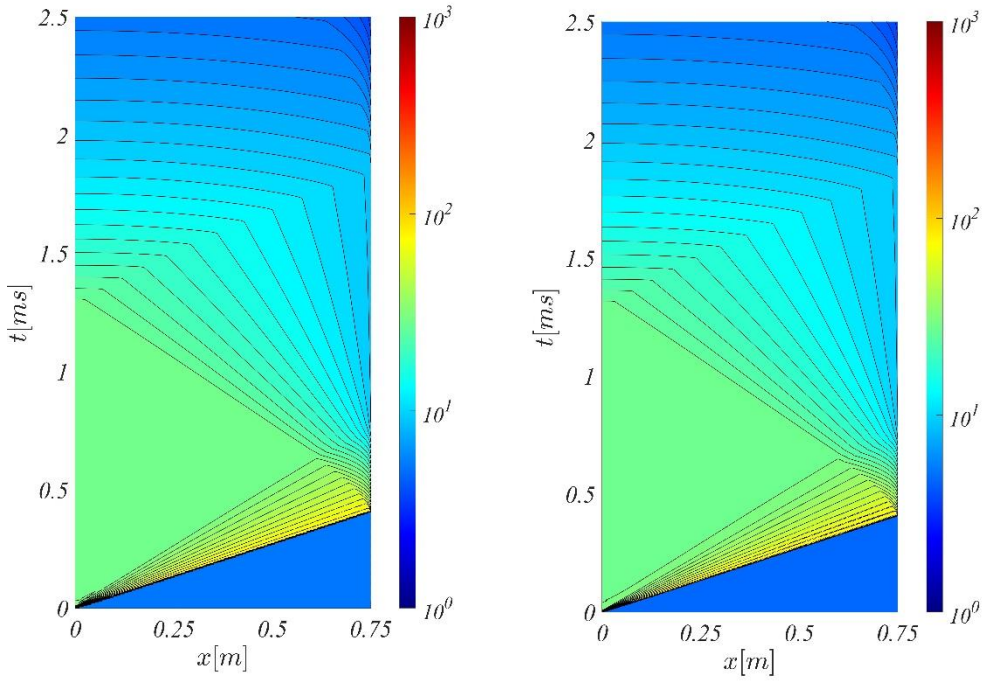

Figure 12. Spatial-temporal pressure field (logarithmic scale) evolution of test case $\boldsymbol{\phi = 0.7}$, $\boldsymbol{L = 0.75}$ m, $\boldsymbol{P_0 = 5.5}$ bar, $\boldsymbol{T_0 = 280}$ K. Comparison of results obtained via CFD (**left**) and data reduction relations (**right**).

5.4. Application Case: Direct Problem

To illustrate a practical application of the direct problem, the following case was chosen: $T_0 = 307$ K, $\phi = 0.7$, $P_0 = 7.3$ bar, $L = 1$ m, $D = 0.07$ m, and $t_{off} = 0.071$ s. This

case was computed via both the CFD and ROM approaches and the obtained results are shown in Table 6. The relative error presented in the table was defined as the absolute value of the ROM result minus the CFD result divided by the CFD result.

Table 6. Comparison of ROM versus CFD results for a specific direct problem case.

Input	ROM	CFD	Error
T_0 [K]	307	307	-
I_T [Ns]	33.6	33.4	0.6%
I_{sp} [m/s]	1629	1645	1%
Freq [Hz]	13.2	13.1	0.7%
E_{max} [N]	93,406	84,053	11%
P_{max} [bar]	109.8	96.6	13.6%
M_T [kg]	0.0206	0.0203	1.5%

Making use of data reduction relations, Figure 13 presents a comparison of the time evolutions of the thrust and mass flow as given by the CFD and the ROM.

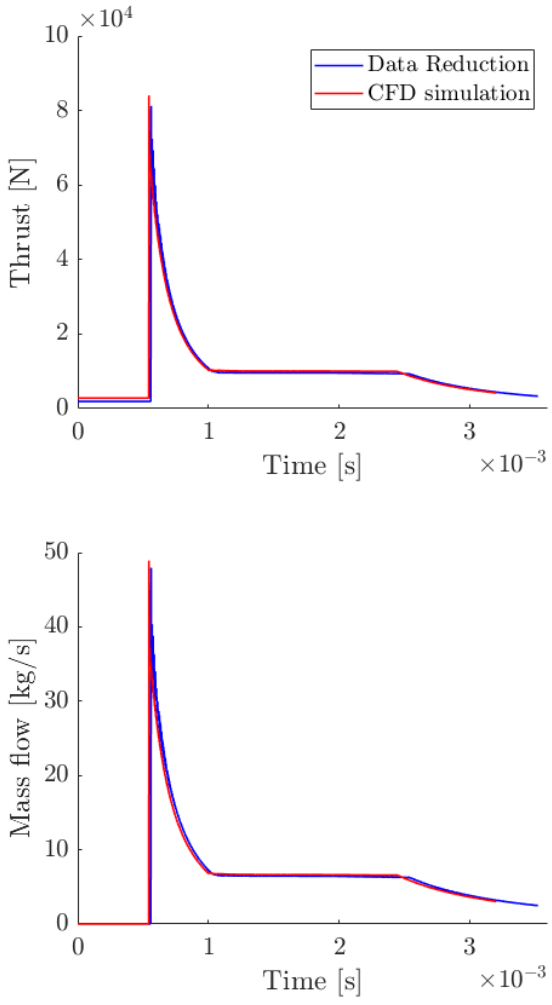

Figure 13. Comparison of time evolutions of thrust and mass flow. Blue line: data reduction. Red line: CFD.

5.5. Application Case: Inverse Problem

Another case was selected to illustrate the practical application of the ROM to the inverse problem. In this case, the chosen performance parameters were: $T_0 = 313$ K, $I_T = 15.5$ Ns, $I_{sp} = 1588$ m/s, $Freq = 22.6$ Hz, $E_{max} = 33166$ N, $P_{max} = 74.5$ bar, and $M_T = 0.009$ kg. The obtained results and the associated errors are presented in Table 7.

Table 7. Comparison of ROM versus exact results for a specific inverse problem case.

Parameter	ROM	Exact	Error
T_0 [K]	313	313	-
ϕ	0.65	0.62	4.8%
P_0 [bar]	5.3	5.8	8.6%
L [m]	1.26	1.20	5%
D [m]	0.051	0.050	2%
t_{off} [s]	0.037	0.038	2.6%

5.6. Discussion

The proposed method has limitations. It is the opinion of the authors that there are to main limitations. The first one is the assumption of 1D flow in the PDE, while the actual setup is 3D. This means that the method should be used in conceptual predesign phases only. Issues such as mixing, discrete injection, etc., cannot be addressed. Simplified models could be developed to consider these effects, but adding further simplifications on top of the main 1D flow idealization may not be practical. The authors think that the workflow used currently in the aerospace industry is adequate. That is: each design phase should have its own design tools with different levels of fidelity and computational load. So, in this sense, extending the present method to 3D cases may not be advisable. The second one is that the maximum amount of information that could be extracted from a limited number of computational cases is limited too. If the database is very sparse, densification via high order singular value decomposition may lead to large errors. The acceptable sparsity threshold could be assessed by the user via monitoring the decomposition eigenmodes.

The mean errors of the proposed methodology, for the direct problem, were of the order of 10%. Obviously, this would not be acceptable in a detailed design phase that was being carried out in an industrial environment. However, this level of uncertainty would be acceptable in an industrial conceptual design phase. In a typical industrial context, the practical objectives of a conceptual design phase are two-fold. The first one is to explore a large multidimensional space of parameters. The second one is to select the most promising subspace that should be passed on to the detailed design phase. Therefore, in this sense, the proposed method may help to achieve the main goal of a conceptual design phase; namely, to help saving time and reducing the cost required for a (potentially very costly) detailed industrial design phase. In this regard, the application cases presented in Sections 5.3–5.5 of the manuscript would be representative cases of the conceptual predesign of a PDE whose parameters are bounded in the 4D space defined in Table 4.

The solution of the inverse problem, as described in Section 4.5 of the manuscript, turned out to be rather robust. Typically, the Latin hypercube sampling technique was used to select the starting point of the optimization process. To test the numerical robustness, some cases were started from points taken at random inside the space of parameters. In these cases, the convergence problem took longer but the final solution was the same. Also, a somewhat unexpected result was the fact that the errors of the inverse problem were of the same order of magnitude as the errors in the direct problem (10%). Given the fact that the input parameters were structured (factorial mesh) while the output parameters were not, larger levels of errors were expected for the inverse problem as compared to the direct problem. However, this proved not to be the case, and the authors were not able to find an explanation. From a practical viewpoint, this is relevant in an industrial context because the method's fidelity is similar for both the performance and design problems, which facilitates the work of engineers.

6. Conclusions

A method has been presented for the performance simulation and conceptual design of rocket-type pulse detonation engines. The method relies on the generation of a high order singular value decomposition reduced-order model. The intended industrial application is in conceptual design phases where large parametric searches need to be carried out both for the direct (performance) and inverse (design) problems. In practice, a requirement for these parametric searches is that they need to be reasonably accurate while keeping a low computational cost.

The methodology that has been presented is generic. However, for the purpose of better illustration, its development has been carried out in the specific context of six input parameters (operation and geometry parameters) and seven output parameters (performance parameters). The output parameters are to be predicted from prescribed input parameters in the direct problem; and the input parameters need to be computed from prescribed output parameters in the inverse problem.

To generate the ROM, a database in tensor form must be populated first. To this end, 480 cases were computed via CFD. The total computational time was 14 days. If the parametric search is to be performed without the aid of a ROM, the number of CFD cases to be run should be more than 10 (possibly hundreds) times higher. This would lead to very large computational times that may interfere with the natural workflow of a conceptual design phase in industry application. In the present study, the ROM that has been generated out of only 480 CFD computations allows for the prediction of performance and operation/geometry parameters with mean errors lower than 10%. Obviously, these errors would not be acceptable in a detailed design phase, but they are admissible during the conceptual design stage. Even more so given the fact that the ROM computational time for a single case is less than a second. This is achieved in the workflow by shifting the heavier computational load (14 days in the present study) off-line. In this way, the user works with the ROM online. Another aspect to be mentioned is the fact that, in the present study, dimensionless data reduction relations were found that facilitate the generation of the ROM. This is not the general case, but if data reduction relations exist, they provide additional benefits regarding the modelization and generalization of the information provided by the CFD. Specifically, appropriate non-dimensionalization allows for the collapse of many different functional relations into single relations that condense, efficiently, a large wealth of information.

In summary, the present approach to the performance simulation and conceptual design of PDEs is based on a reduced-order model obtained from a computational model. In a sense, the authors consider that model-based formulations for the early design phases of these systems are of interest in industrial environments. The reasons are two-fold: (a) at least in the case of PDEs, reasonable fidelity is obtained at a low computational cost, and (b) the existing models allow for easy control of the workflow. Future work may involve testing of the methodology in other propulsion plants.

Author Contributions: Conceptualization. A.V. and E.M., methodology. L.S.d.L. and F.S., software, E.M., F.S. and L.S.d.L., validation. A.V., E.M., F.S. and L.S.d.L., investigation, F.S. and L.S.d.L., writing original draft, A.V., E.M., F.S. and L.S.d.L., writing review, A.V., E.M., F.S. and L.S.d.L., supervision. A.V. All authors have read and agreed to the published version of the manuscript.

Funding: This research was funded by the European Space Agency under contract 4000131302/20/NL/MG.

Data Availability Statement: The datasets presented in this article are not readily available because they are part of an ongoing study. Requests to access the datasets should be directed to the corresponding author.

Acknowledgments: Authors acknowledge the support ptovided by the European Space Agency.

Conflicts of Interest: The authors declare no conflict of interest.

References

1. Buyakofu, V.; Matsuoka, K.; Matsuyama, K.; Kawasaki, A.; Watanabe, H.; Itouyama, N.; Goto, K.; Ishihara, K.; Noda, T.; Kasahara, J.; et al. Development of an S-shaped pulse detonation engine for a sounding rocket. *J. Spacecr. Rocket.* **2022**, *59*, 850–860. [CrossRef]
2. Buyakofu, V.; Matsuoka, K.; Matsuyama, K.; Kawasaki, A.; Watanabe, H.; Itouyama, N.; Goto, K.; Ishihara, K.; Noda, T.; Kasahara, J.; et al. Flight demonstration of pulse detonation engine using sounding rocket S-520-31 in space. *J. Spacecr. Rocket.* **2023**, *60*, 181–189. [CrossRef]
3. Bogoi, A.; Cuciuc, T.; Cojocea, A.V.; Gall, M.; Porumbel, I.; Hriţcu, C.E. Experimental Pressure Gain Analysis of Pulsed Detonation Engine. *Aerospace* **2024**, *11*, 465. [CrossRef]
4. Cojocea, A.V.; Porumbel, I.; Gall, M.; Cuciuc, T. Experimental Thrust and Specific Impulse Analysis of Pulsed Detonation Combustor. *Appl. Sci.* **2024**, *14*, 5999. [CrossRef]
5. Oh, Y.; Choi, M.H.; Park, S. Experimental Investigation of Pulse Detonation Combustion Characteristics via Atomizer Geometry. *Aerospace* **2024**, *11*, 776. [CrossRef]
6. Mattingly, J.D. *Elements of Propulsion: Gas Turbines and Rockets*; American Institute of Aeronautics and Astronautics: Reston, VA, USA, 2006.
7. Ma, F.; Choi, J.Y.; Yang, V. Propulsive performance of airbreathing pulse detonation engines. *J. Propul. Power* **2006**, *22*, 1188–1203. [CrossRef]
8. Wintenberger, E.; Shepherd, J.E. Model for the performance of airbreathing pulse-detonation engines. *J. Propul. Power* **2006**, *22*, 593–603. [CrossRef]
9. Endo, T.; Fujiwara, T. A simplified analysis on a pulse detonation engine model. *T. Jpn. Soc. Aeronaut. S* **2002**, *44*, 217–222. [CrossRef]
10. Mitrofanov, V.V.; Zhdan, S.A. Thrust performance of an ideal pulse detonation engine. *Combust. Explo. Shock+* **2004**, *40*, 380–385. [CrossRef]
11. Allgood, D.; Gutmark, E.; Hoke, J.; Bradley, R.; Schauer, F. Performance studies of pulse detonation engine ejectors. *J. Propul. Power* **2008**, *24*, 1317–1323. [CrossRef]
12. Li, J.L.; Fan, W.; Wang, Y.Q.; Qiu, H.; Yan, C.J. Performance analysis of the pulse detonation rocket engine based on constant volume cycle model. *Appl. Therm. Eng.* **2010**, *30*, 1496–1504. [CrossRef]
13. Paxson, D.E. A simplified model for detonation based pressure-gain combustors. In Proceedings of the 46th AIAA/ASME/SAE/ASEE Joint Propulsion Conference Exhibit, Nashville, TN, USA, 25–28 July 2010. AIAA-2010-6717. [CrossRef]
14. Paxson, D.E.; Kaemming, T. Influence of unsteadiness on the analysis of pressure gain combustion devices. *J. Propul. Power* **2014**, *30*, 377–383. [CrossRef]
15. Chen, W.; Fan, W.; Qiu, H.; Qin, H.; Yan, C. Thermodynamic performance analysis of turbofan engine with a pulse detonation duct heater. *Aerosp. Sci. Technol.* **2012**, *23*, 206–212. [CrossRef]
16. Peace, J.T.; Lu, F.K. Performance modeling of pulse detonation engines using the method of characteristics. *Aerosp. Sci. Technol.* **2019**, *88*, 51–64. [CrossRef]
17. Qiu, H.; Xiong, C.; Li, J. A theoretical and 1-D numerical investigation on a valve/valveless air-breathing pulse detonation engine. *Chinese J. Aeronaut.* **2021**, *34*, 68–78. [CrossRef]
18. Asli, M.; Garan, N.; Neumann, N.; Stathopoulos, P. A robust one-dimensional approach for the performance evaluation of turbines driven by pulsed detonation combustion. *Energ. Convers. Manage.* **2021**, *248*, 114784. [CrossRef]
19. Tan, W.; Zheng, L.; Lu, J.; Xiao, Z. Analysis of Dynamic Operating Characteristics of a Pulse Detonation Turbine Engine. *Aerospace* **2022**, *9*, 550. [CrossRef]
20. Xiao, Z.; Lu, J.; Zheng, L.; Liu, K. Energy and exergy analysis of pulse detonation combustor and pulse detonation turbine engine cycle. *Case Stud. Therm. Eng.* **2024**, *64*, 105426. [CrossRef]
21. Marinov, N.M.; Westbrook, C.K.; Pitz, W.J. Detailed and global chemical kinetics model for hydrogen. *Transp. Phenom. Combust.* **1996**, *1*, 118–129.
22. Gutiérrez Marcantoni, L.G.; Tamagno, J.; Elaskar, S. rhoCentralRfFoam: An OpenFOAM solver for high speed chemically active flows–simulation of planar detonations–. *Comput. Phys. Commun.* **2017**, *219*, 209–222. [CrossRef]
23. Bader, G.; Deuflhard, P. A semi-implicit mid-point rule for stiff systems of ordinary differential equations. *Numer. Math.* **1983**, *41*, 373–398. [CrossRef]
24. Schauer, F.; Stutrud, J.; Bradley, R. Detonation initiation studies and performance results for pulsed detonation engine applications. In Proceedings of the 39th Aerospace Sciences Meeting and Exhibit, Reno, NV, USA, 8–11 January 2001. AIAA-2001-1129. [CrossRef]
25. Wintenberger, E.; Austin, J.M.; Cooper, M.; Jackson, S.; Shepherd, J.E. Analytical model for the impulse of single-cycle pulse detonation tube. *J. Propul. Power* **2003**, *19*, 22–38. [CrossRef]
26. Soloukhin, R.I. *Shock Waves and Detonations in Gases*; Mono Book Corp: Baltimore, MD, USA, 1966.
27. Tucker, L.R. Some mathematical notes on three-mode factor analysis. *Psychometrika* **1966**, *31*, 279–311. [CrossRef]
28. De Lathauwer, L.; De Moor, B.; Vandewalle, J. A multilinear singular value decomposition. *SIAM J. Matrix Anal. A.* **2000**, *21*, 1253–1278. [CrossRef]

29. Byrd, R.H.; Gilbert, J.C.; Nocedal, J. A trust region method based on interior point techniques for nonlinear programming. *Math. Program.* **2000**, *89*, 149–185. [CrossRef]
30. Byrd, R.H.; Hribar, M.E.; Nocedal, J. An interior point algorithm for large-scale nonlinear programming. *SIAM J. Optimiz.* **1999**, *9*, 877–900. [CrossRef]
31. Waltz, R.A.; Morales, J.L.; Nocedal, J.; Orban, D. An interior algorithm for nonlinear optimization that combines line search and trust region steps. *Math. Program.* **2006**, *107*, 391–408. [CrossRef]